Astronomy & Astrophysics manuscript no. output
March 3, 2026

Asteroseismic Analysis of the Merger Product Red Giant in the γ Persei System

Rozália Z. Ádám[1,2], László Molnár[1,2,3], Róbert Szabó[1,2,3], Csilla Kalup[1,2], Frank Grundahl[4], Daniel Huber[5], Mads Skakke Fredslund[4], Pere L. Pallé[6,7], and Dóra Tarczay-Nehéz[1,2]

[1] Konkoly Observatory, Research Centre for Astronomy and Earth Sciences, HUN-REN, MTA Centre of Excellence, Konkoly Thege Miklós út 15-17, H-1121 Budapest, Hungary
e-mail: adam.rozalia@csfk.org
[2] Eötvös Loránd University, Institute of Physics and Astronomy, H-1117 Pázmány Péter sétány 1/A, Budapest, Hungary
[3] MTA–HUN-REN CSFK Lendület "Momentum" Stellar Pulsation Research Group
[4] Stellar Astrophysics Centre (SAC), Department of Physics and Astronomy, Aarhus University, Ny Munkegade 120, DK-8000 Aarhus, Denmark
[5] Institute for Astronomy, University of Hawai'i, 2680 Woodlawn Drive, Honolulu, HI 96822, USA
[6] Instituto de Astrofísica de Canarias, 38200 La Laguna, Tenerife, Spain
[7] Universidad de La Laguna (ULL), Departamento de Astrofísica, 38206 La Laguna, Tenerife, Spain

Received XXX; accepted YYY

ABSTRACT

Context. γ Persei is a long-period eclipsing binary system ($P \approx 14.6$ years) containing a red giant primary, and it is well known for its multi-faceted classification as a visual and spectroscopic binary. Its brightness and binary nature together make it a valuable target for both photometric and spectroscopic studies, particularly in the context of asteroseismology and stellar evolution, as the primary star likely formed through a stellar merger.
Aims. We aim to determine the seismic parameters $\nu_{\rm max}$, $\Delta\nu$, and the oscillation amplitudes of the primary component, an evolved giant, to estimate its seismic mass – which we can compare to its estimated dynamic mass.
Methods. We use Transiting Exoplanet Survey Satellite (TESS) data obtained during Sectors 58, 85, and 86 and to complement the space-based observations, we incorporate high-resolution RV measurements acquired by the Stellar Observations Network Group (SONG) during two distinct epochs; 2017 and 2024.
Results. We successfully detect solar-like oscillations in γ Per and infer a seismic mass of $3.11 \pm 0.12\ M_{\odot}$, which is slightly below the dynamical mass. We find the photometric oscillation amplitudes to be significantly lower than predicted from scaling relations, but in line with other high-mass red giants. We also find that radial velocity amplitudes along the Hertzsprung-Russell diagram cannot be fitted uniformly with current scaling relations.

Key words. asteroseismology – methods: numerical – binaries: eclipsing

1. Introduction

γ Persei is an eclipsing binary system with an almost 15 year-long orbital period, which has been studied from many distinct aspects during the last two century (Campbell 1909; Pourbaix 1999, 2000; Hartkopf et al. 2001; Pourbaix et al. 2004; Piccotti et al. 2020; Diamant et al. 2023). The system is bright enough to be visible to the naked eye with $V = 2.93^m$. Yet, for some time only two primary eclipses were known in the literature, from 1990 by Griffin et al. (1994) and 2019 by Diamant et al. (2023). Recently, Ádám & Molnár (2025) extended this picture by presenting the main eclipse from 2005, and the secondary eclipse from 2006.

The first photometric analysis was done by Griffin et al. (1994), where they published light curves in Johnson U, B and V passbands, and modelled the eclipse geometry. From that they offered radii for both components of the system (22.2 $R_{\odot}$ and 3.9 $R_{\odot}$). While analysing the chromosphere, Diamant et al. (2023) determined new and more precise astrophysical parameters for the system, such as luminosity, effective temperature, surface gravity, radius and mass for primary and secondary.

An interesting aspect of the system was raised by Griffin (2007) and later by Diamant et al. (2023), who found that the components of the system cannot be fitted with a single isochrone. The much younger age of the primary component suggests that the red giant went through a fundamental alteration in its structure and evolution at some point. We investigate a possible merger scenario of two main sequence stars to form the current primary in a companion paper (Tarczay-Nehéz et al. 2026).

Since the primary star of the γ Per system is a red giant, it is expected to show solar-like oscillations. The Transiting Exoplanet Survey Satellite (TESS, Ricker et al. 2015) has been collecting high-precision, continuous photometry from the whole sky, and detected solar-like oscillations in numerous stars across the Hertzsprung–Russell diagram (HRD), permitting population-level asteroseismic studies (e.g., Hon et al. 2021, 2022; Hatt et al. 2023; Zhou et al. 2024; Lund et al. 2025). These stars also include very bright targets, which can be followed up by spectroscopic observations, and their oscillations can be studied in the radial velocity (RV) variations as well, allowing for detailed stellar characterization (e.g., Gupta et al. 2022; Knudstrup

et al. 2023; Kjeldsen et al. 2025; Tang et al. 2026). Though, γ Per was not part of any prior study yet.

In this paper, we aim to obtain a better picture of γ Per by offering independent mass estimates for its red giant primary component through asteroseismic analysis of high-precision photometric and RV observations. In Section 2, first, we present the measurements and facilities we used, then we describe the varied aspects of our analysis. In Section 4 we detail our results and compare γ Per to other oscillating stars with seismic RV data, while in Section 5 we aim to summarize and highlight the importance of our them.

2. Data processing

Continuous, high-precision photometric data was collected by the TESS mission during multiple sectors. RV observations were collected by the Stellar Observations Network Group (SONG) project (Grundahl et al. 2008).

2.1. TESS observations

TESS observes a $24° \times 96°$ degree area of the sky with four 10 cm telescopes nearly continuously for one lunar orbit (27 days). During this time TESS orbits Earth twice, with data download periods during perigee. The field-of-view rotated around the sky with one camera fixed on the ecliptic poles for one year, flipping between the Southern and Northern hemispheres after one year in the early phase in the mission, with different orientations also implemented later on. This observing strategy leads to multiple-sector observations of certain targets where camera pointings can overlap, with long data gaps between repeated visits to the same areas. We processed four visits to γ Per in this work.

TESS observed γ Per during Sector 18 in 2019, which serendipitously coincided with a primary eclipse (Ádám & Molnár 2025). Sector 18 is also the shortest piece of continuous light curve TESS has collected for γ Per: 24.4 days of data, with a 2.5-day gap in the middle. Since during this phase the red giant branch (RGB) component is eclipsing the hotter but smaller secondary star, oscillations are visible unimpeded during the eclipse. We attempted to determine global oscillation parameters from S18, but found the results to be inconclusive.

The space telescope observed the system again during Sector 58 in late 2022, collecting 27.7 days of almost completely continuous data. Since solar-like oscillations are stochastic by nature, short segments may not be representative of the overall seismic profile of the star. Therefore, it is important that we have access to a sector distinct from the S85–86 data, and that we can compare the PSD of the star from different points of time. The PSD of S58 is shown in Figure A.1. Signs of a power excess are visible between 12–28 μHz, which is in agreement with our results based in S85–86 in Section 4.1, but we could not determine a reliable $\nu_{\rm max}$ value from this sector alone.

Finally, γ Per was observed again in Sectors 85 and 86 in late 2024. Sectors 85–86 are the most important for asteroseismology since they provide us with a quasi-continuous light curve that spans 53 days. TESS data are available in multiple forms, including light curves from various pipelines. The processed PDCSAP (pre-search data conditioned simple aperture photometry) light curve released by the TESS Science Processing Operations Center (SPOC) contains multiple gaps in the TESS light curve, where cadences failed various quality cuts, limiting the duty cycle to 61%. In order to limit these gaps, we downloaded the full SAP (simple aperture photometry) light curve that includes every photometric data point. We then manually removed segments most affected by scattered light and large jumps in intensity. The quality of S86 data decreased towards the ends of the orbit: we smoothed the end of the first orbit of S86 to recover the relatively slow variations caused by the oscillations. This increased our temporal coverage significantly, to a duty cycle of 85%. We refer to this latter light curve as our custom light curve throughout the paper. The differences between the two light curves and their PSDs are shown in Fig. 1.

2.2. SONG project

The SONG project aims to study the internal structure and evolution of stars using asteroseismology, such as solar-type oscillations, and to search for and characterize Earth-mass exoplanets. It was launched in 2006 by astronomers at Aarhus University and the University of Copenhagen, and is a mainly Danish-led project. The idea behind the project was to create a network of small telescopes, consisting of eight relatively inexpensive, ultra-modern robotic telescopes.

The first prototype telescope was funded by Danish funds and was installed at the Teide Observatory on Mount Izaña in Tenerife. The Hertzsprung SONG telescope is a 1-meter alt-azimuth Cassegrain telescope manufactured by ASTELCO Systems GmbH. The telescope can switch to another object at speeds of up to 20°/s and has a positional accuracy of less than 3" RMS. The primary mirror is relatively thin, only 5 cm, and has been verified by Shack-Hartmann measurements. The third mirror can be rotated 180°, providing two Nasmyth foci.

The main function of the SONG spectrograph on Tenerife is to determine the radial velocities of stellar surfaces for asteroseismological analyses. It is a high-resolution Echelle spectrograph operating in the resolution range of 35–112 thousand. In normal operation, its resolution is around 100 000. The average dispersion is 0.02 Å/pixel, the measurement range is 4400 – 6900 Å, and the full spectral coverage is below 5300 Å. The detector is a commercial CCD camera designed by Andor and model Ikon-L, with a chip size of 2000×2000. The camera has a high readout speed (3 MHz), which corresponds to a readout time of 2.3 seconds, which helps in measurement efficiency.

The RV measurements we used were obtained in 2017 and 2024 with the Hertzsprung SONG telescope and the SONG spectrograph in Tenerife, Spain. The 2017 observations were targeting γ Per as an asteroseismic target for a possible stellar merger product (PI: Huber). The 2024 observations were proposed to coincide with the TESS observations, in order to be able to compare the RV and photometric asteroseismic signals directly (PI: Molnár). The SONG measurement data is not public. Members of the working groups have access to the light curves and RV curves via SODA[1].

2.2.1. 2017 and 2024 RV data

The 2017 observations consist of three segments covering 128 days, with short gaps between the segments. The data show a slow trend in the RVs, which we fitted and removed with a second-order polynomial. The first 20 days of the campaign were observed in high cadence mode with up to 250 measurements per night. Data taken after that are typically on the order of a dozen observations per night.

Somewhat surprisingly, the first segment, including the high-cadence observations, displays a strong beating pattern instead

[1] https://soda.phys.au.dk/

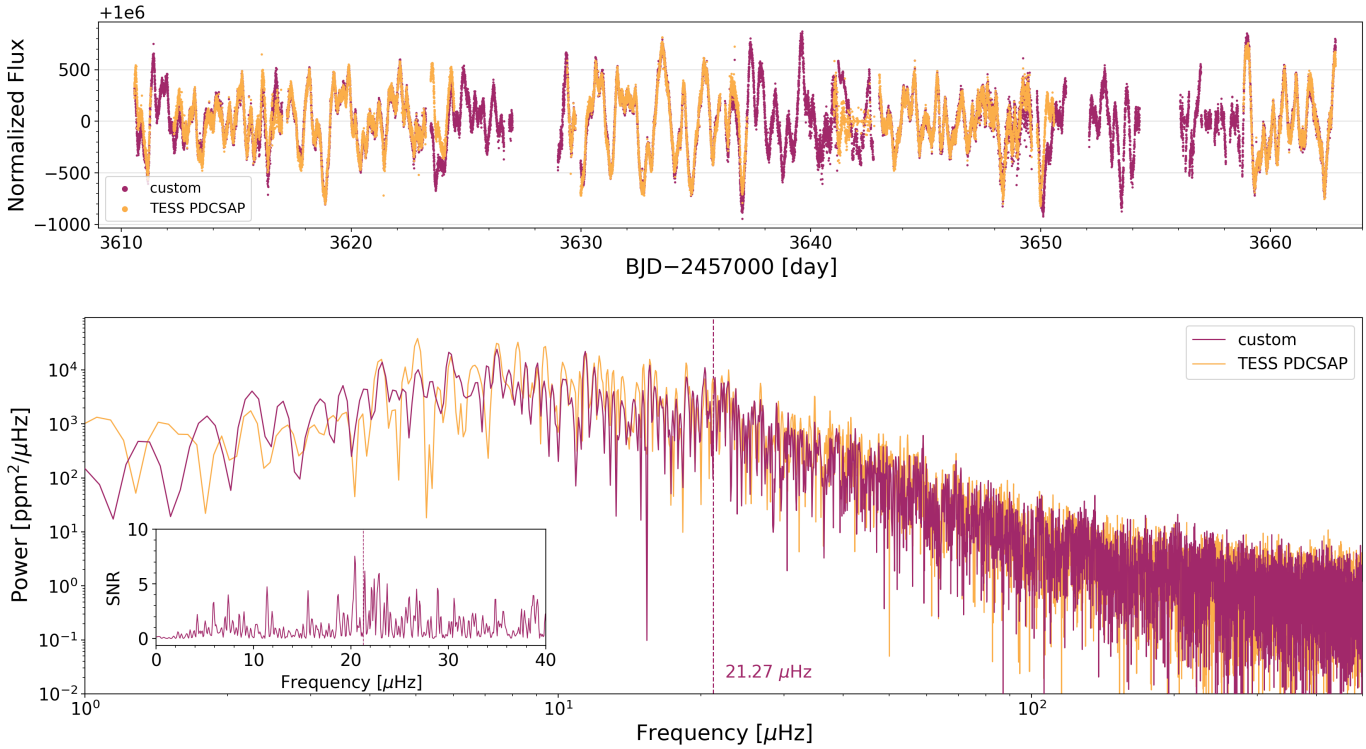

Fig. 1. We produced two light curves from data points collected by TESS in Sectors 85 and 86. *Top:* our custom light curve with magenta, and the downloadable PDCSAP light curve with orange. *Bottom:* the power spectral density (PSD) of these light curves with the respective colours, and with an inset of the SNR of the PSD of the custom light curve.

of the usual, semi-regular variations around typical periodicities and amplitudes. This beating then subsides, and the low-cadence part shows far less amplitude variations.

A peculiarity of the early 2017 data is that the frequency spectrum shows strong signals close to integer frequencies 1.0, 2.0, 3.0... d^{-1} (Fig. 2). This makes the determination of the true frequency content especially difficult. Even with observations spanning full nights, the RV curve can be folded either with the 1.0 or 2.0 d^{-1} frequency due to the limited phase coverage. We note that the fact that peaks in the frequency spectrum coincide with the alias peaks in the spectral window of the data does not mean that signals are not real, or that they are only caused by the sampling of the data, although such claims have been made in the literature occasionally. Mathematically, the frequency spectrum is the convolution of the window function and the actual physical signals in the data. Therefore, any significant peak in the frequency spectrum requires an observed signal. We are merely left with an ambiguous spectrum with confusion between true frequencies and aliases. We show the solution to this puzzle in Sect. 3.3.

The 2024 observing campaign was designed to be contemporaneous with the TESS S85–86 measurements. Observations ran from 2024-11-26 to 2024-12-16, but the first week was mostly lost to bad weather. Useful data was collected from day 5, resulting in a 17 d long data set, coinciding with S86. Long-term RV changes were once again removed with a second-order polynomial fit.

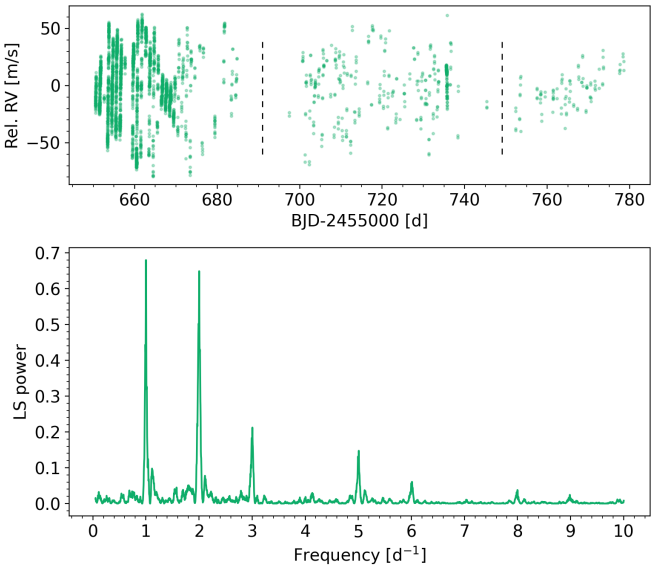

Fig. 2. SONG RV measurements of γ Per during the 2017 campaign. *Top:* the complete data set with dashed lines marking the separation between the dense, and the middle and late sparse data segments. *Bottom:* the power spectrum of the data set, showing strong daily aliasing.

2.2.2. Gaussian Processes interpolation of the RV data

We fitted the RV data with Gaussian Processes (GPs) to create continuous representations that approximate the behaviour of the signal. We used the `tinygp` python package (Foreman-Mackey et al. 2024) for this purpose.

We used a simple harmonic oscillator (SHO) kernel to fit the data (Foreman-Mackey et al. 2017). As the cadence of the measurements and the shape of the RV curve both changed considerably during the 2017 measurements, we split the data into

three segments and fitted them separately. We left the σ scaling parameter at 1.0, and set the initial frequency to $\omega = 2\pi\,2.0$, based on $\nu_{\rm max}$ (Section 4) and the strongest frequency of $2.0\,d^{-1}$ we found in the frequency spectrum.

The individual segments are short relative to the expected lifetime of the modes. We found that an underdamped oscillator with a high Q quality factor gave us the best result. For the 2024 data, we chose $Q = 10$, and for the 2017 data segments we tried multiple values. For the first, better-sampled segment we show both $Q = 9$ and 10 to produce two alternate fits in Fig. B.1. For the sparser segments we tested two fits again, this time with both $Q = 18$ and 20, because lower Q values tended to converge to solutions around $\sim 1.0\,d^{-1}$ dominant frequency. For the middle we show the $Q = 18$ and 20 fits, and for the last segment a $Q = 20$ fit in Figs. B.2.

We also included a jitter term to account for the white noise present in the data by adding an extra term the diagonal elements of the covariance matrix ($\sigma_{jitter} = 0.45$). We extracted the maximum likelihood model and created an interpolated curve for the time span of each segment. We then compared the PSD of these models to the PSD of the observed RV data segments.

Models of the 2017 data are displayed in Fig. B.1, their respective PSDs used for amplitude calculation are shown in Figs. B.3 and B.4. The fit for the 2024 data is shown in the upper panel of Fig. 3, where green dots refer to the observations, the green shaded area refer to uncertainty of the `tinygp` model, and the green line indicates the maximum likelihood model. As the figures show, both the oscillation signals were reproduced well by the GP models. At the same time the granulation background became more visible, although the model could be oversmoothing the highest frequency range.

3. Asteroseismic analysis

Our main aim was to characterize the solar-like oscillations in γ Per A, and to derive the physical parameters of the RGB component through asteroseismic analysis. This can be achieved in two ways. One is peakbagging, i.e., determining the frequencies of individual modes and comparing those to oscillation frequencies of stellar models. We found the TESS light curves to be too short for this type of analysis. The other way is to determine the global characteristics of the oscillation spectrum, and use scaling relations to infer stellar parameters. In this latter case, our aim is to determine the parameters $\nu_{\rm max}$, the frequency of maximum oscillation power, and $\Delta\nu$, the average large frequency separation between successive radial mode orders.

3.1. Scaling relations

Scaling relations for $\Delta\nu$ and $\nu_{\rm max}$ were first proposed by Ulrich (1986) and Brown et al. (1991), respectively, and then summarized by Kjeldsen & Bedding (1995). They showed that asteroseismic parameters of other stars can be inferred by scaling the solar values based on relations between solar and stellar mass, radius and effective temperature (or, alternatively, luminosity) values. Kallinger et al. (2010) rearranged these equations to infer stellar masses, in various forms:

$$\frac{M}{M_\odot} = \left(\frac{\nu_{\rm max}}{\nu_{\rm max,\odot}}\right)^3 \left(\frac{\Delta\nu}{\Delta\nu_\odot}\right)^{-4} \left(\frac{T}{T_\odot}\right)^{1.5} \tag{1}$$

$$\frac{M}{M_\odot} = \left(\frac{\Delta\nu}{\Delta\nu_\odot}\right)^2 \left(\frac{L}{L_\odot}\right)^{1.5} \left(\frac{T}{T_\odot}\right)^{-6} \tag{2}$$

$$\frac{M}{M_\odot} = \left(\frac{\nu_{\rm max}}{\nu_{\rm max,\odot}}\right) \left(\frac{L}{L_\odot}\right) \left(\frac{T}{T_\odot}\right)^{-3.5} \tag{3}$$

$$\frac{M}{M_\odot} = \left(\frac{\nu_{\rm max}}{\nu_{\rm max,\odot}}\right)^{2.4} \left(\frac{\Delta\nu}{\Delta\nu_\odot}\right)^{-2.8} \left(\frac{L}{L_\odot}\right)^{0.3} \tag{4}$$

Since γ Per A is a RGB star, we used correction factors for both $\Delta\nu$ and $\nu_{\rm max}$. The $\Delta\nu$ correction factor is described by Sharma et al. (2016) as

$$f_{\Delta\nu} = \left(\frac{\Delta\nu}{135.1\ \mu\text{Hz}}\right) \left(\frac{\rho}{\rho_\odot}\right)^{-0.5}, \tag{5}$$

where 135.1 μHz corresponds to their adopted choice for $\Delta\nu_\odot$. Since we have a red giant star with an unclear density, we assumed a multiplier of 0.97 for $\Delta\nu_\odot$ based on Figure 4 of Sharma et al. (2016). The correction factor for $\nu_{\rm max}$ is presented by Pinsonneault et al. (2025) in Eq. (4) as

$$f_{\nu_{\rm max}} = (1 + p)^{-1}, \tag{6}$$

where

$$p = a\,(\ln \nu_{\rm max})^3 + b\,(\ln \nu_{\rm max})^2 + c\,(\ln \nu_{\rm max}) + d, \tag{7}$$

whose a, b, c and d parameters are based on models published by Sharma et al. (2016) and presented in Table 2 in Pinsonneault et al. (2025). For the custom light curve we got $f_{\nu_{\rm max}} = 1.002505$, while for the PDCSAP light curve we derived $f_{\nu_{\rm max}} = 1.001285$. We note that there are more recent works on the subject, e.g., Li et al. (2023) derived a more sophisticated formula with respect to stellar properties, but their work unfortunately does not cover the higher-mass range.

For our calculations we presumed 10% error for the $\nu_{\rm max}$ and $\Delta\nu$ pair based on the fractional error histograms by Stello et al. (2022) and the assumption that systematic errors arise due to the shortness of the dataset.

3.2. PySYD analysis

We estimated initial values for $\nu_{\rm max}$ and $\Delta\nu$ from the TESS data with the built-in asteroseismology module of `lightkurve` (Lightkurve Collaboration et al. 2018) first. More accurate values, however, require more sophisticated tools. Therefore, we subsequently analysed the light curves with the `pySYD` software (Chontos et al. 2022). This tool was specifically developed to determine the global asteroseismic parameters from the power spectra of solar-like oscillators. After an initial fit it masks the detected (or input) region around the power excess, and fits the granulation background with multi-component Harvey-like functions (Harvey 1985). It then subtracts the background model, and determines $\nu_{\rm max}$ from a heavily smoothed power spectrum. The $\Delta\nu$ parameter is determined from the autocorrelation function of the background-subtracted spectrum. For low SNR power excesses, `pySYD` often struggles with instabilities during the Monte Carlo sampling routine, which causes it to fail. We therefore applied a more stable linear background model for

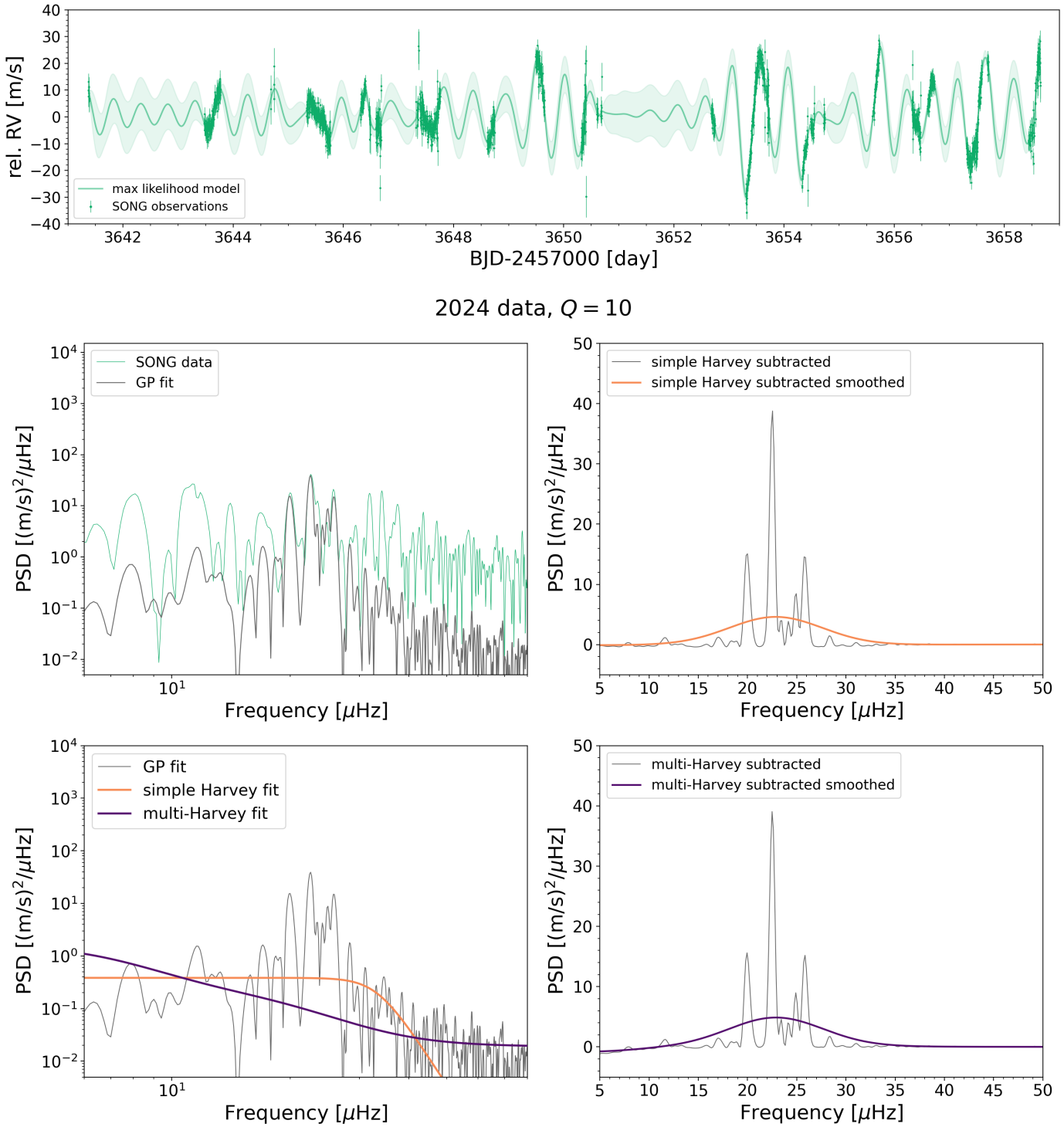

Fig. 3. SONG observations from the 2024 campaign. *Top panel:* we interpolated the data using the `tinygp` code whose maximum likelihood model is shown with a green line, the light green area refer to standard deviation of the model, while the observations are denoted with green dots. *Middle left panel:* the PSD of the interpolated 2024 data (GP fit) with grey, compared to the PSD of the original observations in green. *Bottom left panel:* the same PSD of the interpolated 2024 data with grey shown with the granulation background fits; a Harvey-like function with orange line, and a multi-component Harvey-like function with purple. *Middle and bottom right panels:* we display the PSD after subtracting the simple Harvey background fit in grey in the upper plot and PSD after subtracting the multi-component Harvey in the lower one. The orange and purple lines refer to smoothed PSDs, respectively.

the power excess envelope, as introduced for M4 oscillating red giant stars by Howell et al. (2022).

The search range for $\Delta\nu$ is limited based on the $\nu_{\rm max}$–$\Delta\nu$ scaling relation (Stello et al. 2009). However, the exact form of this scaling relation is sensitive to evolutionary stage and stellar mass. Since γ Per is known to be a high-mass red giant, we used a scaling relation of $\Delta\nu = 0.24\,{\nu_{\rm max}}^{0.75}$ to define the search range, based on the findings of Huber et al. (2011). `PySYD` can estimate

uncertainties of both parameters by Monte Carlo-sampling the calculated posterior distributions for the parameters. We discuss the results in Section 4.1 along with the mass estimates.

3.3. Aliasing in the 2017 SONG data

As we described above, the RV data starts out in a peculiar manner, dominated by a beating pattern. The peaks in the power spectrum are very close to 1.0, 2.0 and 3.0 d^{-1}, with the 2.0 d^{-1} (23.15 μHz) peak being the strongest. This could suggest that the true signal is at 2.0 d^{-1}, but daily aliasing makes this conclusion uncertain. We first analysed this beating section of the data set, up until BJD2457685. A classical prewhitening analysis indicates close-by peaks at 2.0037 and 1.9454 d^{-1}, creating the beating pattern. Once we removed these, the power spectrum of the residual RV curve displayed a low-amplitude, wide power excess between 1.0 and 4.0 d^{-1}, much more reminiscent of a solar-like oscillator.

Still, we were left with an ambiguous frequency solution, because a beating of two frequencies at 1.0 d^{-1} (11.57 μHz) fits the data nearly equally well. However, here we can break this ambiguity thanks to the TESS observations, which place ν_{max} to ≈ 22 μHz, as we show in the next Section. Thus, we can assume that the 2.0 d^{-1} peak is the true signal, and we can proceed with the analysis from there.

4. Results

The detection of the oscillation power excess in γ Per allows us to estimate the asteroseismic mass of the primary, and to compare it to classical mass inferences. Moreover, with the SONG data at hand we can extend RV seismology into the RGB regime, and investigate how this star relates to already characterized smaller, main sequence (MS) and subgiant (SG) stars.

4.1. Seismic parameters and mass estimates

We calculated mass estimates as described in Section 3.1 based on the global seismic parameters we determined. Following the steps described in Section 3.2, we derived a pair of ν_{max} and $\Delta\nu$ values. Analysing the custom light curve, we got ν_{max} = 21.27 ± 0.98 μHz and $\Delta\nu$ = 2.31 ± 0.10 μHz. This light curve, as well as its PSD are shown in the two panels of Fig. 1. The respective coloured dashed line in the lower panel refer to the derived ν_{max} value.

Based on the $\Delta\nu$ values we obtained, we investigated the echelle diagram of the data using the `echelle` python package (Hey & Ball 2020). We found that a value of $\Delta\nu$ = 2.44 μHz gave the best visual result, as shown in the right panel of Fig. 4. Although the frequency resolution of the data is low, we were able to construct an echelle diagram that shows a repetition of peaks on the left side, at the even mode orders (ℓ = 0 and 2), and a scatter of peaks on the right side, where ℓ = 1 mixed modes are expected. The `pySYD` $\Delta\nu$ value of 2.307 μHz gives a similar result (left panel of Fig. 4), but with the largest-amplitude peak appearing among the odd modes.

The scatter among the odd modes can be explained by the presence of mixed modes (Beck et al. 2011; Basu & Hekker 2020; Lindsay et al. 2022). The ℓ = 1 p modes are coupled to ℓ = 1 g modes in the core, and this causes deviations from the expected ridge, as weakly coupled modes stay close to the $\Delta\nu$ frequency spacing, but strongly coupled modes follow the $\Delta\Pi$ period spacing of g modes more closely instead. Given the low frequency resolution and the low SNR levels of the PSD, we did not attempt to fit individual peaks in the data.

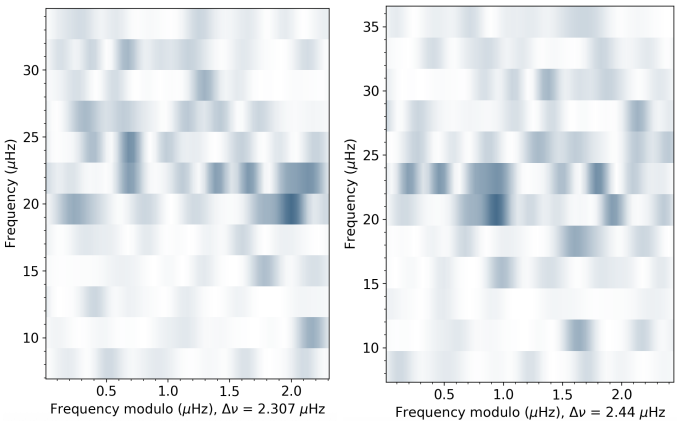

Fig. 4. Echelle diagrams of the SNR spectrum of the TESS S85–S86 custom photometry (shown in magenta in Fig. 1), using $\Delta\nu$ = 2.307 μHz, based on the `pySYD` analysis, and $\Delta\nu$ = 2.44 μHz, based on visual inspection of the echelle diagrams, respectively.

We used two values for $\nu_{max,\odot}$; 3141 μHz (Andersen et al. 2019) and 3050 μHz (Kjeldsen & Bedding 1995), since no consensus has been reached, and it also changes over the solar cycle. We applied $\Delta\nu_\odot$ = 135.1 μHz based on Huber et al. (2011). For the solar temperature we adopted the IAU sanctioned value: $T_\odot$ = 5772 K (Prša et al. 2016a). Finally, for γ Per A we adopted T = 4970 K and $L = 10^{2.45}$ $L_\odot$ from Diamant et al. (2023). The results are in shown in Table 1 and Fig. 5. As in Fig. 1, the results based on the custom light curve are shown with orange, while the ones based on the PDCSAP light curve are magenta. The triangles show the calculations with $\nu_{max,\odot}$ = 3141 μHz, the squares with $\nu_{max,\odot}$ = 3050 μHz. The grey area refer to the dynamical mass (and its error) derived by Diamant et al. (2023).

The inferred mass values for each scaling relationship are listed in Table 1, and shown in Fig. 5. We computed the inverse-variance weighted means of the values for both $\Delta\nu$ values. For the `pySYD` value ($\Delta\nu$ = 2.307 μHz), our result is M_{seism} = 3.11 ± 0.12 $M_\odot$, which we accept as the primary result. For the alternate, visually estimated $\Delta\nu$, the same averaging technique gives $M_{seism,alt}$ = 3.24 ± 0.13 $M_\odot$.

4.2. Photometric amplitudes

Solar-like oscillations are stochastic by nature, so individual mode amplitudes vary over time – as the 2017 SONG data clearly demonstrates. Therefore, if we want to characterize the strength of the oscillations, we need to calculate averaged amplitudes per oscillation modes, as defined by Kjeldsen et al. (2008).

The first steps in their method is to heavily smooth the power excess in the PSD with a Gaussian filter and to remove the background signal coming from granulation noise. We followed Kjeldsen et al. (2008) and set the FWHM (full width at half maximum) of the Gaussian to be 4$\Delta\nu$ for the smoothing. Since the power excess has a low SNR, we used multiple methods to test the robustness of our amplitude values. First, we fitted the granulation background in the TESS data with a single Harvey-like function, originally developed to describe granulation noise in solar data (Harvey 1985). This was followed by fitting a more complex model with multiple Harvey-functions using MCMC, while excluding the modes themselves within the region of the power excess. After removing the background

Seismic parameters	$\nu_{\max,\odot}$ [μHz]	$M(\nu_{\max}, \Delta\nu, T)$ [$M_\odot$]	$M(\Delta\nu, L, T)$ [$M_\odot$]	$M(\nu_{\max}, L, T)$ [$M_\odot$]	$M(\nu_{\max}, \Delta\nu, L)$ [$M_\odot$]	$\bar{M}$ [$M_\odot$]
$\nu_{\max} = 21.268 \pm 0.98$ μHz, $\Delta\nu = 2.307 \pm 0.100$ μHz	3141	2.92 ± 0.65	3.89 ± 0.41	3.22 ± 0.22	3.01 ± 0.49	3.11 ± 0.12
	3050	3.19 ± 0.71		3.32 ± 0.22	3.22 ± 0.53	
$\nu_{\max} = 21.268 \pm 0.98$ μHz, $\Delta\nu = 2.44 \pm 0.10$ μHz	3141	2.33 ± 0.50	3.79 ± 0.45	3.22 ± 0.22	2.57 ± 0.41	3.24 ± 0.13
	3050	2.55 ± 0.55		3.32 ± 0.22	2.76 ± 0.44	

Table 1. Seismic mass estimations (with errors) derived from four different scaling relations using the $\nu_{\max}$ determined from our custom light curve. In the first line $\Delta\nu$ is also derived from our custom light curve, while its value in the second line is based on visual inspection of the echelle diagrams (see Fig. 4).

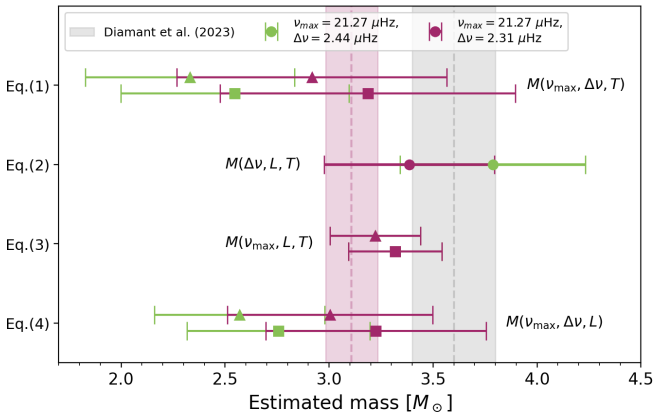

Fig. 5. We plotted the results of the mass estimation calculations over the dynamical mass range (grey) published by Diamant et al. (2023). Magenta, like earlier, refers to seismic masses determined based on the $\nu_{\max}, \Delta\nu$ pair derived from the custom light curve, while for green we used the same $\nu_{\max}$ with the visually determined $\Delta\nu = 2.44$ μHz. Note that Eq. (3) uses only $\nu_{\max}$ and thus results are identical for both cases. The triangles show the mass calculated with $\nu_{\max,\odot} = 3141$ μHz, while the squares refer to $\nu_{\max,\odot} = 3050$ μHz. The magenta area displays our estimated mass range.

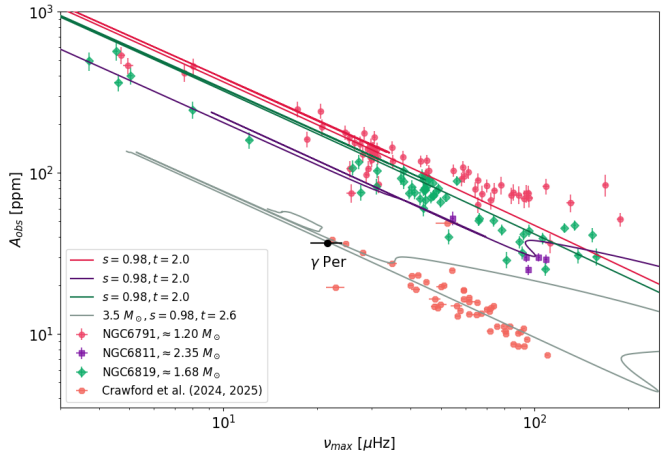

Fig. 6. Comparison of the measured average mode amplitudes between γ Per A (black dot) and the three open clusters in the original *Kepler* FoV (pink, purple and green dots) by Stello et al. (2011), and other high-mass *Kepler* stars (orange) published by Crawford et al. (2024) with updated masses from Crawford et al. (2025). Models with lines in respective colours of the open clusters and grey from MIST.

signal, we smoothed the PSD with the sliding Gaussian filter described above. The two different background fits resulted in small differences and gave us additional handles on the amplitude uncertainties.

The average amplitude is calculated from the peak value of the smoothed PSD. In the last step, Kjeldsen et al. (2008) multiplies this value with $\Delta\nu/c$ to obtain the average amplitude per oscillation mode, where c is a factor that measures the effective number of modes per order. The value of c depends on the sensitivity of the observations to the various low-degree modes. This sensitivity will be different both for the method we use (photometry or RVs), and for the wavelength range of the photometric observations, as well. For TESS observations, we used $c = 2.95$ (Kjeldsen et al. 2008).

In the case of γ Per, we also have to account for the binary nature of the star. Based on the luminosities published by Diamant et al. (2023), we calculate the dilution factor of the luminosity of γ Per A to be $(L_A + L_B)/L_A = 1.24$. Finally, since we are interested in the bolometric amplitudes, we also calculated the bolometric correction factor for the luminosity to be $c_{P-bol} = 1.0395$, as defined by Lund (2019) for the equation $A_{bol} = c_{P-bol} A_P$. With these corrections implemented, we arrive to an average bolometric luminosity amplitude per oscillation mode of $A_{bol} = 36.6 \pm 1.5$ ppm.

Originally, Kjeldsen & Bedding (1995) derived that oscillation amplitudes scale by $A_{bol} = (L/M)(T_{eff,\odot}/T_{eff})A_{bol,\odot}$. This means that higher-mass red giants at the same luminosity (or $\nu_{\max}$) level will have lower amplitudes, which is nicely illustrated if we compare γ Per to a similar but lower-mass star. For HD 145250, for example, even single-sector observations provided stronger power excess detections, despite being a fainter target (Molnár & Lelkes 2025). However, the scaling relation of Kjeldsen & Bedding (1995) would predict amplitudes on the order of ≈ 300 ppm for γ Per A, which is still an order of magnitude higher than what we see with TESS.

Since we cannot model mode amplitudes for oscillations numerically, validating the scaling relation requires comparison of observed amplitudes with physical parameters of real stars. This has been investigated multiple times, mostly based on *Kepler* observations. Stello et al. (2011), for example, compared the mode amplitudes of three open clusters within the original *Kepler* field-of-view (FoV) to estimates based on isochrones fitted to the clusters, adding exponents to the L/M and T_{eff} scaling. They found a good agreement between the observed and predicted slopes of the A_{bol}–$\nu_{\max}$ relation, but the observations revealed a clear mass-related separation, which the scaled models did not reproduce. Based on a larger sample of field stars in the *Kepler* FoV, Huber et al. (2011) further refined the amplitude scaling, adding separate exponents to L and M, to account for the observed stronger mass dependence.

We plot the open cluster data from Stello et al. (2011) in Fig. 6, with the estimated average masses indicated, and along with with $A_{\rm bol}$–$\nu_{\rm max}$ relations based on MIST isochrones (MESA Isochrones and Stellar Tracks, Choi et al. 2016; Dotter 2016) interpolated to the ages and metallicities of the clusters. We tested the scaling defined by Huber et al. (2011) and found that the L and M scaling exponents $s = 0.98$ and $t = 2.0$, reproduces the cluster observations the closest. We then added oscillation amplitudes published by Crawford et al. (2024, 2025), who specifically targeted heavier red giants above 2.5 $M_\odot$ in the *Kepler* field. We also included a stellar track at $M = 3.5\,M_\odot$ with modified scaling exponents of $s = 0.98$ and $t = 2.6$ that align with γ Per A and the higher-mass *Kepler* stars. Figure 6 clearly shows that the observed amplitude of the star, as well as all the other high-mass stars, are significantly lower than the predicted value based on the mass scaling relation of Kjeldsen & Bedding (1995), in agreement with the conclusions of Crawford et al. (2024). This further suggests that the scaling relations need to be modified to describe the amplitudes of more massive stars accurately.

4.3. Oscillation amplitudes from RVs

We also calculated the average amplitude per oscillation mode from the RV data. We again followed the method of Kjeldsen et al. (2008). Unlike our earlier photometric analysis, here we did not need to account for the binarity. We used an effective mode number coefficient of $c = 4.09$, and the same background removal and smoothing process as described in Section 4.2. The main deviation from the photometry is that we used the PSDs of the GP models instead of the PSDs of the actual RV data. We did this to prevent aliasing from influencing our calculations. As we described in Section 2.2.1, the GP model PSDs reproduce the oscillation signals well.

The fit for the GP model of the 2024 data is shown in the upper section of Fig. 3; the 2017 fits are shown in the Appendix in two panels of Fig. B.1. Based on these fits, the average RV amplitude of γ Per A is between 170 ± 30 (2024 data) and 590 ± 60 m/s (first segment of the 2017 data). The various RV amplitudes are listed in Table 2, which were derived from their PSDs as shown in Figs. 3, B.3, B.4, B.5, B.6 and B.7. The average RV amplitude is significantly higher than the RV amplitudes measured for MS and SG stars which are in the 0.02–0.65 m/s range (Kjeldsen et al. 2008; Campante et al. 2024). Our observation then leads to an important question: which amplitude scaling relation extends into the RGB/red clump (RC) regime correctly? Kjeldsen & Bedding (1995) originally proposed a simple $A_{\rm vel} \propto (L/M)^s$ relation with $s = 1.0$. Theoretical models and observations put the exponent to $s = 0.7$–1.5 (Houdek et al. 1999; Samadi et al. 2005), with observations favouring the higher end of the range (Campante et al. 2024).

We compiled a list of stars for which oscillation parameters ($\nu_{\rm max}$, $\Delta\nu$, $A_{\rm vel}$), $T_{\rm eff}$, and mass values have been published (see Table C.1). Where only approximate values were provided for $\nu_{\rm max}$, we assumed a 10% uncertainty. We show the distribution of $A_{\rm vel}$ amplitudes against $T_{\rm eff}$, colour-coded by $\log \nu_{\rm max}$ in Fig. 7. The distribution of the points clearly reproduce the HRD, with most of the stars forming the MS, three stars falling onto the SG branch (β Aql, ν Ind, HD35833), and γ Per A falling on the RGB. γ Per A is shown with two dots connected by a line, as we determined two values for its $A_{\rm vel}$ (Sect. 4.3). We plot also includes four stellar evolutionary tracks from the MIST database. Three of these show theoretical $T_{\rm eff}$ and $A_{\rm vel}$ values for non-rotating, solar-metallicity models with masses of $M = 0.7$, 1.0, and 1.3 $M_\odot$. The fourth line is a stellar track representing

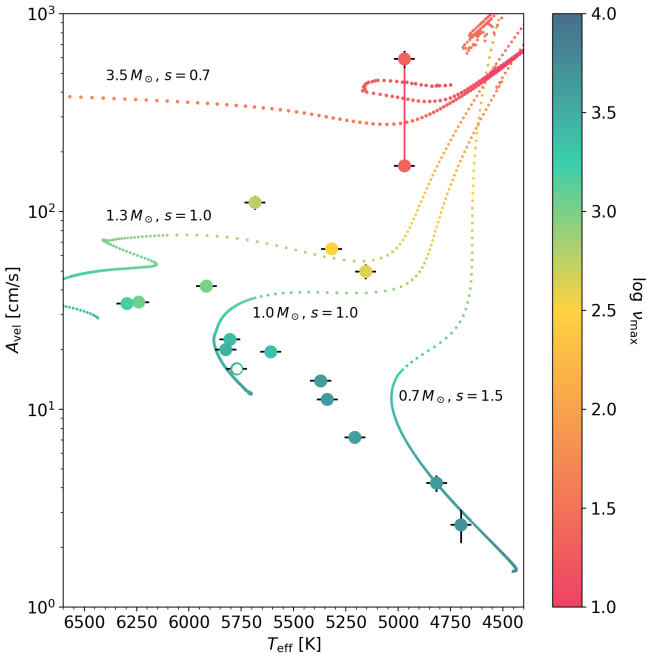

Fig. 7. The distribution of $A_{\rm vel}$ amplitudes against $T_{\rm eff}$, colour-coded by $\log \nu_{\rm max}$. The evolutionary tracks follow four different initial stellar masses, and change colour according to their $\log \nu_{\rm max}$. The exponents we used in the $A_{\rm vel}$ scaling relations are also indicated. The HRD is clearly visible with most of the stars forming the MS, three stars falling onto the SG branch (β Aql, ν Ind, HD35833), and γ Per A falling on the RGB or RC. The Sun is marked with an empty circle.

γ Per A, at $M = 3.5\,M_\odot$ and [Fe/H] = −0.2. As noted in the plot, we used different s values as well, between 0.7 and 1.5.

We then plotted the same stars onto the $\nu_{\rm max}$–$A_{\rm vel}$ plane in Fig. 8, this time colour-coded with stellar mass. This plot also includes a set of stellar evolutionary tracks from the MIST database. Four tracks show theoretical $\nu_{\rm max}$ and $A_{\rm vel}$ values for non-rotating, solar-metallicity models with masses of $M = 0.7$, 0.8, 1.0, and $1.2 M_\odot$. The fifth line is a stellar track representing γ Per A, at $M = 3.5\,M_\odot$ and [Fe/H] = −0.2. We calculate $\nu_{\rm max}$ from Eq. (3), and the RV amplitudes as:

$$A_{\rm vel} = (L/M)^s\, A_{\rm vel,\odot}. \tag{8}$$

Two sets of lines show the difference between the two extrema of the amplitude scaling, at $s = 0.7$ (dashed lines) and 1.5 (solid lines) in Fig. 8.

As the plot shows, stars near the Sun (displayed with a diamond) can be fitted with either exponent reasonably well. Away from the Sun, differences become clearer. The stars ϵ Ind and HD35833 can only be fitted by the highest, $s = 1.5$ exponent, the former which is in agreement with the findings of Campante et al. (2024). In contrast, the two SG stars, β Aql A and ν Ind, as well as γ Per A require lower exponents. For the 3.5 $M_\odot$ track in particular (purple dashed line), we only show the 0.7 scaling, because if we use the 1.5 exponent the values shift into the ~ 100 m/s range, and run well outside of the plotted area. Unfortunately, Knudstrup et al. (2023) did not publish the amplitudes for γ Cep A, which would probe the split between exponents further at $\nu_{\rm max} = 186\,\mu$Hz. Our results indicate that the exponent of the RV amplitude scaling should feature another parameter dependence, such as $\log g$ or R, to account for the differences in slope for non-solar-like stars.

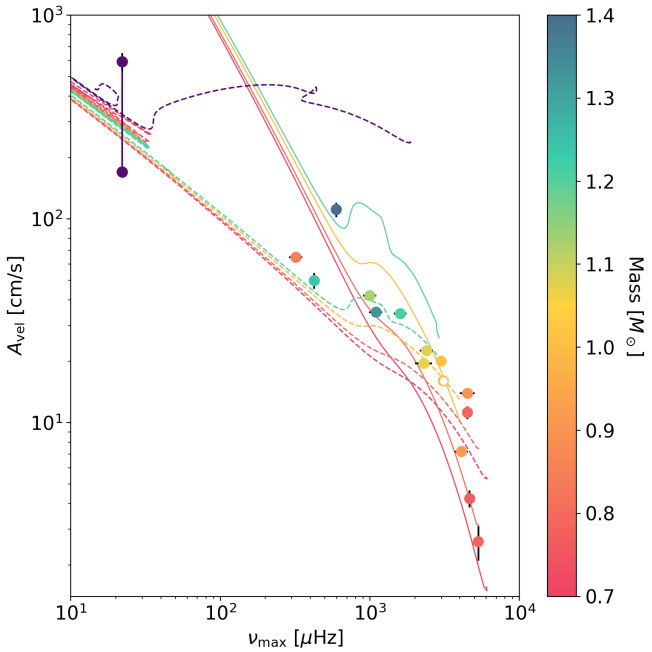

Fig. 8. Same comparison as in Fig. 7 on the ν_{max}–A_{vel} plane, this time colour-coded with stellar mass. Here, the same coloured evolutionary tracks differ with amplitude scaling, dashed lines refer to $(L/M)^{0.7}$, while solid lines $(L/M)^{1.5}$. Sun is shown with an empty circle.

Table 2. The RV amplitude per oscillation mode values we determined based on GP fits with different quality factors applied to specific data sections.

Data segment	A_{vel} [cm/s]
2017 dense data, $Q = 9$	590 ± 60
2017 dense data, $Q = 10$	470 ± 50
2017 sparse data, part 1, $Q = 18$	420 ± 60
2017 sparse data, part 1, $Q = 20$	310 ± 50
2017 sparse data, part 2, $Q = 20$	210 ± 30
2024 data, $Q = 10$	170 ± 30

4.4. Ratio of photometric and RV amplitudes

Just like the frequency parameters of the oscillations, ν_{max} and $\Delta\nu$, scale with the physical parameters of stars, so do the oscillation amplitudes. Scaling relations for intensity and RV amplitudes were proposed by Kjeldsen & Bedding (1995), and were refined in their later work (Kjeldsen & Bedding 2011). These relations predict that the ratio of the bolometric intensity and RV amplitudes scale inversely with the effective temperature of the star: $A_{bol}/v_{osc} \sim T_\odot/T_{eff}$, which can be tested against the solar value.

Since the 2024 TESS and SONG observations were taken contemporaneously, we can calculate the RV to luminosity amplitude ratio for γ Per. The solar ratio is $A_{bol,\odot}/A_{vel,\odot} = 19.5 \pm 0.7$ ppm/ms^{-1}. For γ Per we calculate this ratio to be $A_{bol}/v_{bol} = 21.5 \pm 0.2$ ppm/ms^{-1}. The ratio between the solar and γ Per values is 1.10 ± 0.04. Since the (inverse) ratio of the effective temperature of γ Per against the Sun is 1.16 ± 0.02, and we expect the oscillation amplitude ratios to scale with that, as Fig. 9 shows, the A_{bol}/A_{vel} value we got agrees with the expected value within 1.4σ. We also find good agreement with the amplitude ratio of

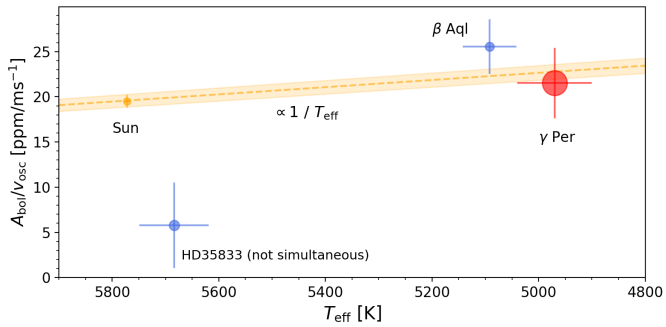

Fig. 9. We determined the average oscillation amplitude per mode quantities A_{bol} and v_{osc} for the light curve and RV data following Kjeldsen et al. (2008). We find that their ratio follows the expected $1/T_{eff}$ scaling as predicted by Kjeldsen & Bedding (1995). Here, we show a comparison with two other stars. Point sizes correspond to stellar mass.

β Aql, based on the results of Kjeldsen et al. (2025). Another star, for which photometric and RV oscillations have been determined in the same way, is HD35833 (Gupta et al. 2022). This star is offset from the expected ratio, but these measurements were not contemporaneous and could indicate a change in oscillation amplitudes over time, as well.

5. Discussion and conclusions

In this paper we carried out the first asteroseismic analysis of the bright RGB primary component of the γ Persei system, based on photometry collected by TESS, and infer a seismic mass of $= 3.11 \pm 0.12\,M_\odot$. We also detected the oscillations in RVs from measurements collected with SONG. Sadly, even after obtaining simultaneous observations by TESS and SONG from 2024, we cannot compare them directly, as both are too sparse, especially the SONG data. Despite, we were able to determine the mode-averaged oscillations amplitudes both from photometry and from RVs.

After comparing our mass and amplitude values with literature data, we can state that γ Per A clearly does not fit the results for open clusters published by Stello et al. (2011) in Fig. 6; the photometric amplitude appears to be too low. However, it perfectly aligns with the high-mass stars published by Crawford et al. (2024, 2025). Therefore, we conclude that the amplitude scaling must have a much steeper mass dependence at higher masses, possibly with $t = 2.6$. Fast rotation and strong magnetic activity can inhibit solar-like oscillations (Chaplin et al. 2011; Gaulme et al. 2014; Mathur et al. 2019), and simulations show that mergers can create highly magnetic massive blue straggler stars (Schneider et al. 2019). However, they subsequently spin down, and their magnetic fields may weaken by the time they evolve to the RGB. Being a likely MS-MS merger product (Tarczay-Nehéz et al. 2026) seems to have no effect on its own on the photometric oscillation amplitudes of γ Per as it fits perfectly among other oscillating high-mass red giants. Resolving the conundrum of low amplitudes in massive RGB stars therefore will require further observations, including magnetic field strength or chromospheric activity indicator measurements (Gehan et al. 2024).

Considering the HRD formed by stars with RV oscillation amplitude data in Fig. 7, γ Per falls right where expected, on the RGB. Thus, we could argue that we are in the right range of A_{vel} value. We also note that according to our findings, a different

exponent needed for red giants regarding the $A_{\rm vel}$ scaling relation to MS and SG stars.

Studying the $\nu_{\rm max}$–$A_{\rm vel}$ plane in Fig. 8, we see that γ Per prefers the evolutionary track scaled with $(L/M)^{0.7}$, and aligns even with low-mass stars. We do not have enough comparison stars to argue for either set of tracks. Most of them, just like our red giant, follow the dashed lines and $s = 0.7$ scaling. On the other hand, the lowest and highest (other than γ Per) mass stars suggest evolutionary tracks scaled with $(L/M)^{1.5}$. As the study of evolutionary tracks is not scope of this paper, we shall not go into further detail – though, we note it is a matter worth investigating.

As discussed in Section 4.4, our results of γ Per are in good agreement with the expected $1/T_{\rm eff}$ scaling of the photometric and RV amplitude ratio. Though, Fig. 9 is in dire need of further data points, ergo stars for which both $A_{\rm bol}$ and $v_{\rm osc}$ are determined, preferably contemporaneously, in order to argue the validity of this relation.

Overall, γ Per highlights the importance of studying high-mass red giant stars, and validates the effort needed to collect RV data for red giant oscillators. While several such stars are potentially accessible by TESS, RV observations require more extensive efforts. One target in particular which would be amenable to a similar analysis is α UMa, which is brighter and appears to be even heavier than γ Per A (Buzasi et al. 2000; Rudrasingam et al. 2026).

Acknowledgements. R. Z. Á. and L. M. would like to thank Daniel Hey and Benjamin Pope for discussions on Gaussian Processes fitting. Cs. K. would like to thank Madeline Howell for her help with implementing the linear background fitting model in `pySYD` and for providing a more suitable approach to estimate global seismic parameters and their their uncertainties for low-frequency, low-SNR stars. Cs. K. would also like to thank Oliver Hall for his help in creating an automated MCMC background fitting model for analysing low-amplitude solar-like oscillators. This research was supported by the 'SeismoLab' KKP-137523 Élvonal grant and the NKFIH excellence grant TKP2021-NKTA-64 of the Hungarian Research, Development and Innovation Office (NKFIH). This project received funding from the LP2025-14/2025 Lendület grant of the Hungarian Academy of Sciences. This paper includes data collected with the TESS mission, obtained from the MAST data archive at the Space Telescope Science Institute (STScI). Funding for the TESS mission is provided by the NASA Explorer Program. STScI is operated by the Association of Universities for Research in Astronomy, Inc., under NASA contract NAS 5–26555. This research made use of NASA's Astrophysics Data System Bibliographic Services, as well as of the SIMBAD and VizieR databases operated at CDS, Strasbourg, France.

References

Ádám, R. Z. & Molnár, L. 2025, AJ, 169, 196
Aguilera-Gómez, C., Ramírez, I., & Chanamé, J. 2018, A&A, 614, A55
Akeson, R., Beichman, C., Kervella, P., Fomalont, E., & Benedict, G. F. 2021, AJ, 162, 14
Andersen, M. F., Pallé, P., Jessen-Hansen, J., et al. 2019, A&A, 623, L9
Basu, S. & Hekker, S. 2020, Frontiers in Astronomy and Space Sciences, 7, 44
Bazot, M., Ireland, M. J., Huber, D., et al. 2011, A&A, 526, L4
Beck, P. G., Bedding, T. R., Mosser, B., et al. 2011, Science, 332, 205
Bedding, T. R., Butler, R. P., Carrier, F., et al. 2006, ApJ, 647, 558
Bedding, T. R., Kjeldsen, H., Arentoft, T., et al. 2007, ApJ, 663, 1315
Brown, T. M., Gilliland, R. L., Noyes, R. W., & Ramsey, L. W. 1991, ApJ, 368, 599
Buzasi, D., Catanzarite, J., Laher, R., et al. 2000, ApJ, 532, L133
Campante, T. L., Kjeldsen, H., Li, Y., et al. 2024, A&A, 683, L16
Campbell, W. W. 1909, ApJ, 29, 224
Carrier, F. & Eggenberger, P. 2006, A&A, 450, 695
Carvalho-Silva, G., Meléndez, J., Rathsam, A., et al. 2025, ApJ, 983, L31
Chaplin, W. J., Bedding, T. R., Bonanno, A., et al. 2011, ApJ, 732, L5
Choi, J., Dotter, A., Conroy, C., et al. 2016, ApJ, 823, 102
Chontos, A., Huber, D., Sayeed, M., & Yamsiri, P. 2022, The Journal of Open Source Software, 7, 3331
Crawford, C. L., Bedding, T. R., Li, Y., et al. 2024, MNRAS, 528, 7397
Crawford, C. L., Li, Y., Huber, D., et al. 2025, MNRAS, 542, 3289
Diamant, S. J. M., Schröder, K. P., Jack, D., et al. 2023, A&A, 674, A162
Dotter, A. 2016, ApJS, 222, 8
Foreman-Mackey, D., Agol, E., Ambikasaran, S., & Angus, R. 2017, AJ, 154, 220
Foreman-Mackey, D., Yu, W., Yadav, S., et al. 2024, dfm/tinygp: The tiniest of Gaussian Process libraries
Fouesneau, M., Frémat, Y., Andrae, R., et al. 2023, A&A, 674, A28
Fuhrmann, K. & Chini, R. 2021, MNRAS, 501, 4903
Gaulme, P., Jackiewicz, J., Appourchaux, T., & Mosser, B. 2014, ApJ, 785, 5
Gehan, C., Godoy-Rivera, D., & Gaulme, P. 2024, A&A, 686, A93
Griffin, R. E. 2007, in IAU Symposium, Vol. 240, Binary Stars as Critical Tools & Tests in Contemporary Astrophysics, ed. W. I. Hartkopf, P. Harmanec, & E. F. Guinan, 645–649
Griffin, R. F., Griffin, R. E. M., Snyder, L. F., et al. 1994, International Amateur-Professional Photoelectric Photometry Communications, 57, 31
Grundahl, F., Christensen–Dalsgaard, J., Arentoft, T., et al. 2008, Communications in Asteroseismology, 157, 273
Gupta, A. F., Luhn, J., Wright, J. T., et al. 2022, AJ, 164, 254
Hartkopf, W. I., Mason, B. D., & Worley, C. E. 2001, The Astronomical Journal, 122, 3472
Harvey, J. 1985, in ESA Special Publication, Vol. 235, Future Missions in Solar, Heliospheric & Space Plasma Physics, ed. E. Rolfe & B. Battrick, 199
Hatt, E., Nielsen, M. B., Chaplin, W. J., et al. 2023, A&A, 669, A67
Hekker, S. 2020, Frontiers in Astronomy and Space Sciences, Volume 7 - 2020
Hey, D. & Ball, W. 2020, Echelle: Dynamic echelle diagrams for asteroseismology
Hojjatpanah, S., Figueira, P., Santos, N. C., et al. 2019, A&A, 629, A80
Hon, M., Huber, D., Kuszlewicz, J. S., et al. 2021, ApJ, 919, 131
Hon, M., Kuszlewicz, J. S., Huber, D., Stello, D., & Reyes, C. 2022, AJ, 164, 135
Houdek, G., Balmforth, N. J., Christensen-Dalsgaard, J., & Gough, D. O. 1999, A&A, 351, 582
Howell, M., Campbell, S. W., Stello, D., & De Silva, G. M. 2022, MNRAS, 515, 3184
Huber, D., Bedding, T. R., Stello, D., et al. 2011, ApJ, 743, 143
Kallinger, T., Weiss, W. W., Barban, C., et al. 2010, A&A, 509, A77
Karovicova, I., White, T. R., Nordlander, T., et al. 2022, A&A, 658, A47
Kjeldsen, H. & Bedding, T. R. 1995, A&A, 293, 87
Kjeldsen, H. & Bedding, T. R. 2011, A&A, 529, L8

Kjeldsen, H., Bedding, T. R., Arentoft, T., et al. 2008, ApJ, 682, 1370
Kjeldsen, H., Bedding, T. R., Li, Y., et al. 2025, A&A, 700, A39
Knudstrup, E., Lund, M. N., Fredslund Andersen, M., et al. 2023, A&A, 675, A197
Li, Y., Bedding, T. R., Stello, D., et al. 2023, MNRAS, 523, 916
Li, Y., Huber, D., Ong, J. M. J., et al. 2025, ApJ, 984, 125
Lightkurve Collaboration, Cardoso, J. V. d. M., Hedges, C., et al. 2018, Lightkurve: Kepler and TESS time series analysis in Python, Astrophysics Source Code Library
Lindsay, C. J., Ong, J. M. J., & Basu, S. 2022, ApJ, 931, 116
Lund, M. N. 2019, MNRAS, 489, 1072
Lund, M. N., Chontos, A., Grundahl, F., et al. 2025, A&A, 701, A285
Lundkvist, M. S., Kjeldsen, H., Bedding, T. R., et al. 2024, ApJ, 964, 110
Mathur, S., García, R. A., Bugnet, L., et al. 2019, Frontiers in Astronomy and Space Sciences, 6, 46
Metcalfe, T. S., van Saders, J. L., Huber, D., et al. 2024, ApJ, 974, 31
Molnár, L. & Lelkes, K. 2025, Research Notes of the American Astronomical Society, 9, 137
Piccotti, L., Docobo, J. Á., Carini, R., et al. 2020, MNRAS, 492, 2709
Pinsonneault, M. H., Zinn, J. C., Tayar, J., et al. 2025, ApJS, 276, 69
Pourbaix, D. 1999, Astronomy and Astrophysics, 348, 127
Pourbaix, D. 2000, A&AS, 145, 215
Pourbaix, D., Tokovinin, A. A., Batten, A. H., et al. 2004, A&A, 424, 727
Prša, A., Harmanec, P., Torres, G., et al. 2016a, AJ, 152, 41
Prša, A., Harmanec, P., Torres, G., et al. 2016b, AJ, 152, 41
Ricker, G. R., Winn, J. N., Vanderspek, R., et al. 2015, Journal of Astronomical Telescopes, Instruments, and Systems, 1, 014003
Rosenthal, L. J., Fulton, B. J., Hirsch, L. A., et al. 2021, ApJS, 255, 8
Rudrasingam, J., Bedding, T. R., Pope, B. J. S., et al. 2026, arXiv e-prints, arXiv:2602.22472
Samadi, R., Goupil, M.-J., Alecian, E., et al. 2005, Journal of Astrophysics and Astronomy, 26, 171
Santos, N. C., Israelian, G., & Mayor, M. 2001, A&A, 373, 1019
Schneider, F. R. N., Ohlmann, S. T., Podsiadlowski, P., et al. 2019, Nature, 574, 211
Sharma, S., Stello, D., Bland-Hawthorn, J., Huber, D., & Bedding, T. R. 2016, ApJ, 822, 15
Soubiran, C., Brouillet, N., & Casamiquela, L. 2022, A&A, 663, A4
Soubiran, C., Creevey, O. L., Lagarde, N., et al. 2024, A&A, 682, A145
Stello, D., Chaplin, W. J., Basu, S., Elsworth, Y., & Bedding, T. R. 2009, MNRAS, 400, L80
Stello, D., Huber, D., Kallinger, T., et al. 2011, ApJ, 737, L10
Stello, D., Saunders, N., Grunblatt, S., et al. 2022, MNRAS, 512, 1677
Tang, J., Wang, S. X., Li, Y., et al. 2026, arXiv e-prints, arXiv:2601.14076
Tarczay-Nehéz, D., Molnár, L., & Ádám, R. 2026, arXiv e-prints, arXiv:2602.00896
Teixeira, T. C., Kjeldsen, H., Bedding, T. R., et al. 2009, A&A, 494, 237
Ulrich, R. K. 1986, ApJ, 306, L37
Zhou, J., Bi, S., Yu, J., et al. 2024, ApJS, 271, 17

Appendix A: TESS Sector 58 PSD and S85–86 custom light curve

To include as many TESS sectors as possible, in this section we present the PSD of TESS S58 PDCSAP light curve (see Fig. A.1), which we discuss in Section 3.2. The inset of plot shows the mentioned power excess.

The first 10 lines of our custom light curve for TESS S85–86 is in Table A.1, which is shown with orange in the upper panel of Fig. 1.

Table A.1. Sample table of the custom light curve of TESS S85–86. The full table is available in machine-readable format in the electronic version.

BJD–2450000 (days)	Normalised flux (ppm)	Flux error (ppm)
3610.559580	1000270.395155	23.905707
3610.560969	1000257.896040	23.905972
3610.562358	1000291.292855	23.905575
3610.563747	1000289.284790	23.905590
3610.565136	1000300.270852	23.906213
3610.566525	1000273.825517	23.906836
3610.567914	1000363.728699	23.907461
3610.569303	1000315.707129	23.907508
3610.570692	1000321.091593	23.906256
3610.572080	1000321.231168	23.906539
...		

Appendix B: Interpolation of the SONG 2017 data

As described in Section 2.2.1, the 2017 SONG RV data was dominated by a beating pattern and strong daily aliasing, which we aimed to resolve by Gaussian Processes interpolation as detailed in Section 2.2.2.

We first divided the data into three segments, one dense and two sparse ones as shown in Fig. 2. Nevertheless, even the dense section was too sparse for a definite `tinygp` fit, consequently the two most likely solutions are shown in Fig. B.1 (with Q = 9.0 and 10.0). Likewise, we provided models for the two sparse sections in Fig. B.2, specifically two for the part 1 with Q = 18.0 and Q = 20, and one for part 2 with Q = 20.0.

Like the middle and bottom panel of Fig. 3, the PSDs of the original data and the GP models are presented green and dark grey lines in the left panels, respectively, and the orange lines show the granulation background fit with single Harvey function, the purple ones are ourmulti-component Harvey-like functions fit in Figs. B.3, B.4, B.6, B.5, and B.7. On the right panels we present GP model PSDs after subtracting each background model, and the results of the Gaussian smoothing are shown with thick orange and purple lines for each.

Appendix C: Stars used for comparison

To check the validity of our results, we compared the derived parameters to other published ones. Since these values are scattered among several different works, we collected the parameters of these stars in Table C.1 with their respective references, which we hope will help future investigations in the this field.

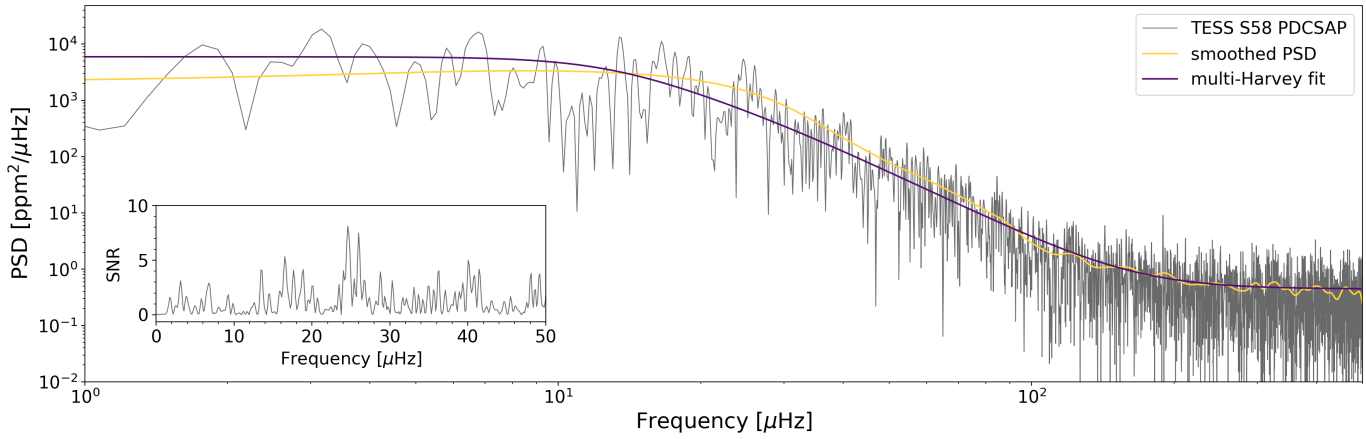

Fig. A.1. The PSD of TESS Sector 58 PDCSAP light curve is shown with grey, the smoothed version is plotted over with yellow, the multi-component Harvey-like functions fit is with purple. The inset displays the SNR of the PSD.

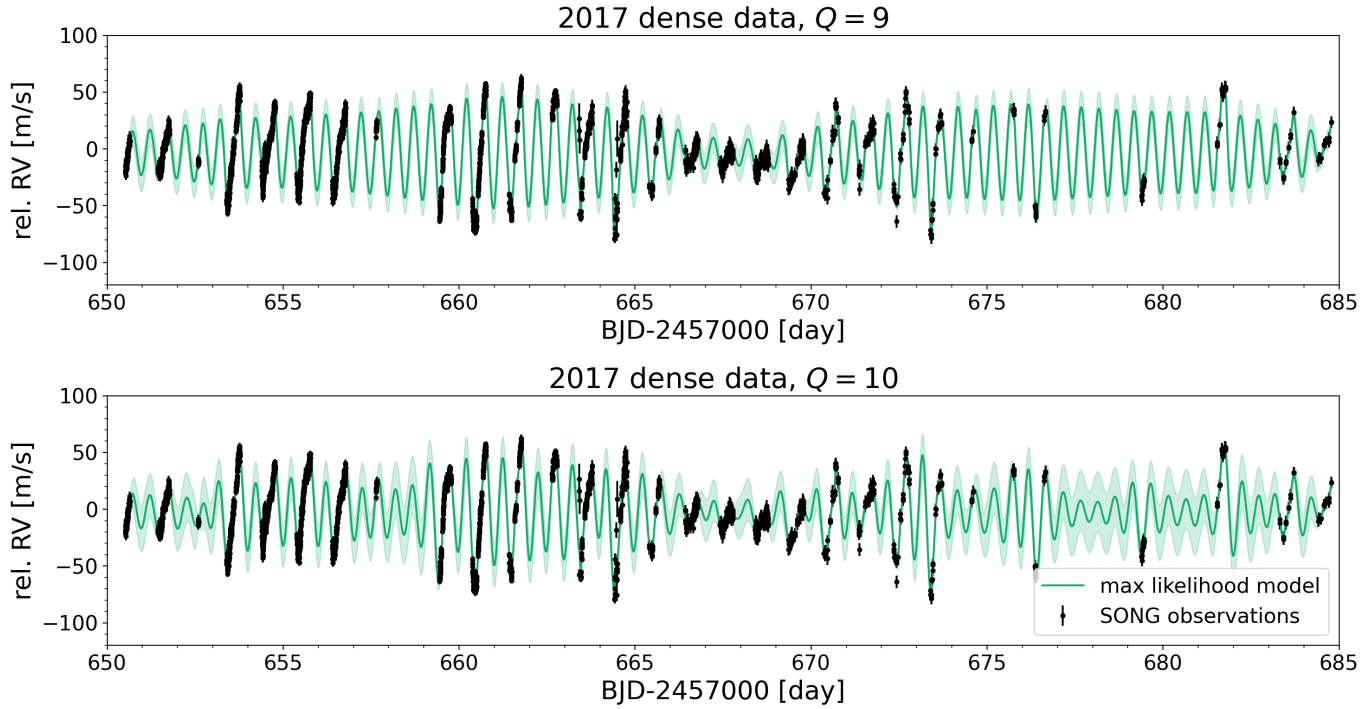

Fig. B.1. Two solutions for the `tinygp` fit of 2017 dense SONG observations (black dots). The maximum likelihood model is shown with green lines, while green shaded area refers to the standard deviation of the model.

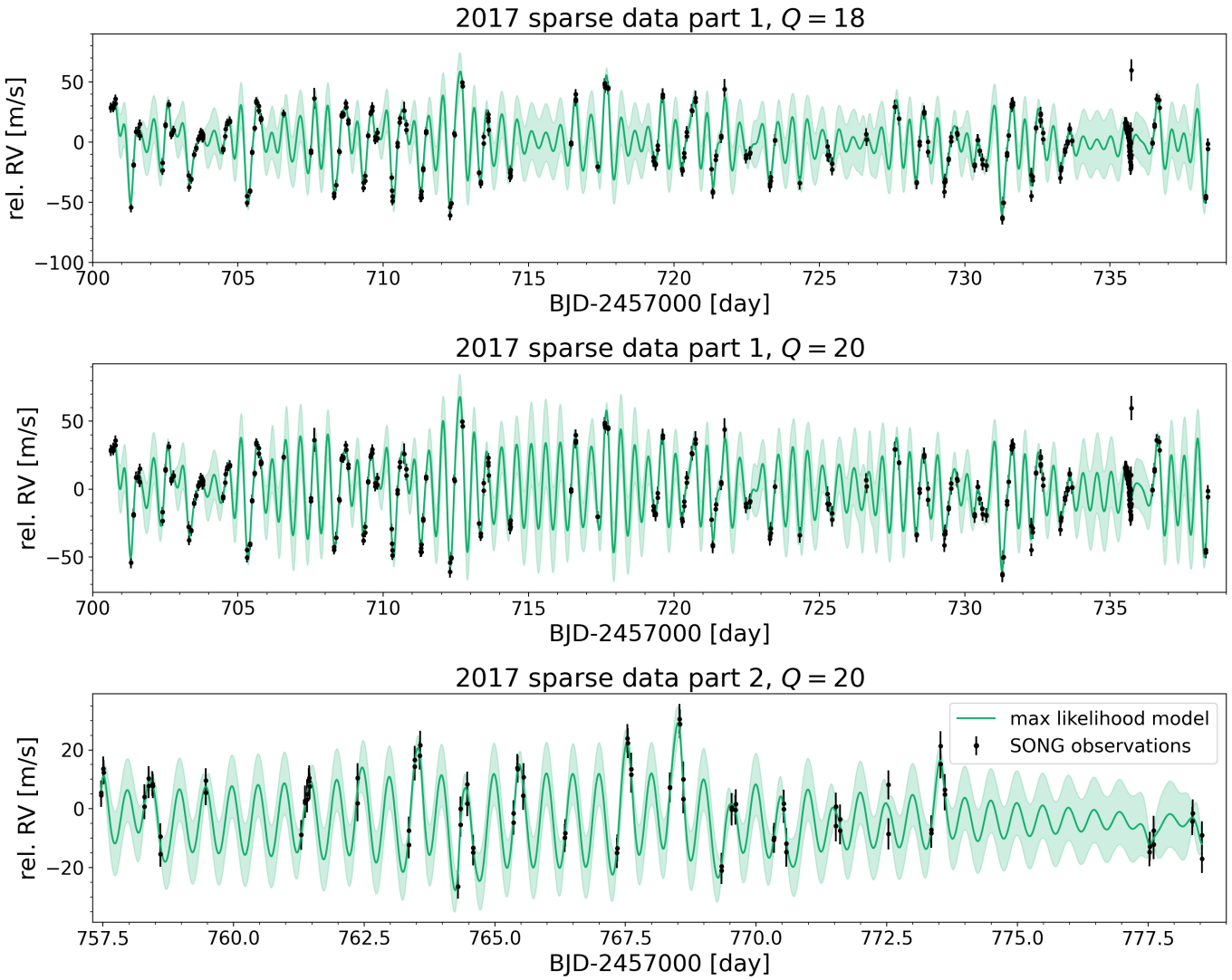

Fig. B.2. The first two panels present `tinygp` fits of the first part of the sparse section of the 2017 SONG observations. The bottom plot shows fit of the sparse section part 2 of the 2017 campaign. In all cases the black dots are the SONG observations, the maximum likelihood model is shown with green lines, while green shaded area refers to the standard deviation of the model.

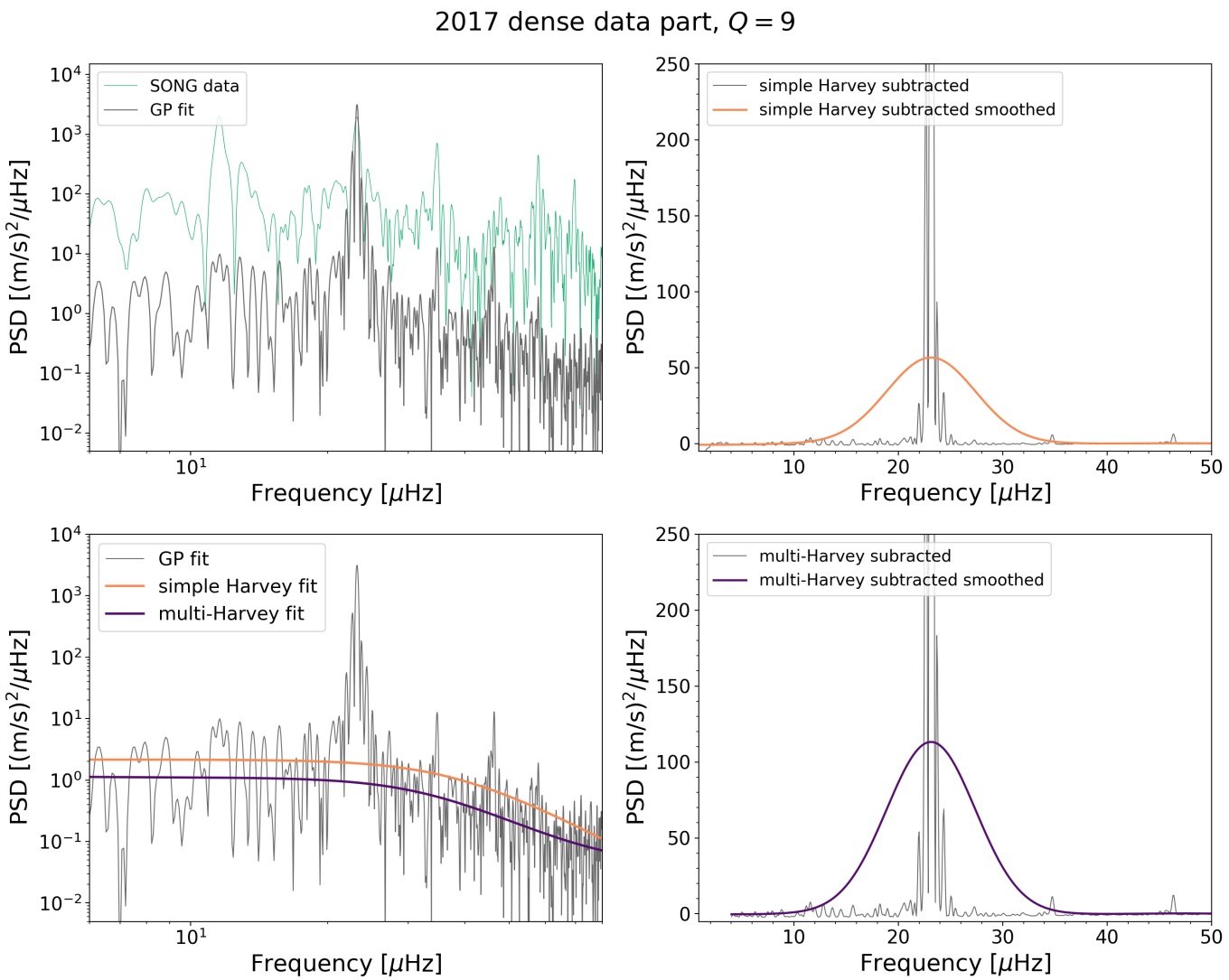

Fig. B.3. PSDs of first solution for the SONG 2017 dense segment with background fits. Grey lines correspond to the `tinygp` model in the top plot of Fig. B.1.

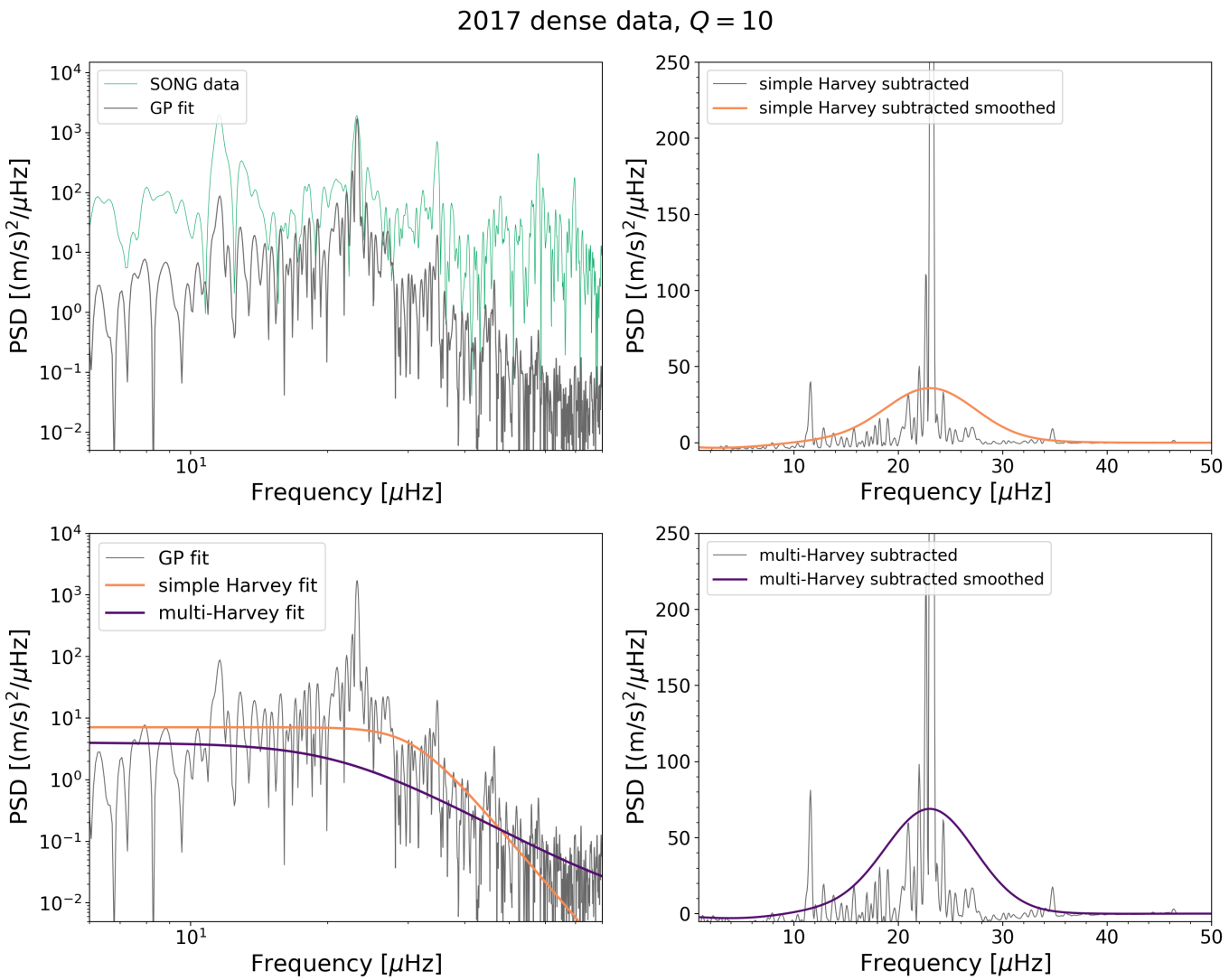

Fig. B.4. PSDs of second solution for the SONG 2017 dense segment with background fits. Grey lines correspond to the `tinygp` model in the bottom plot of Fig. B.1.

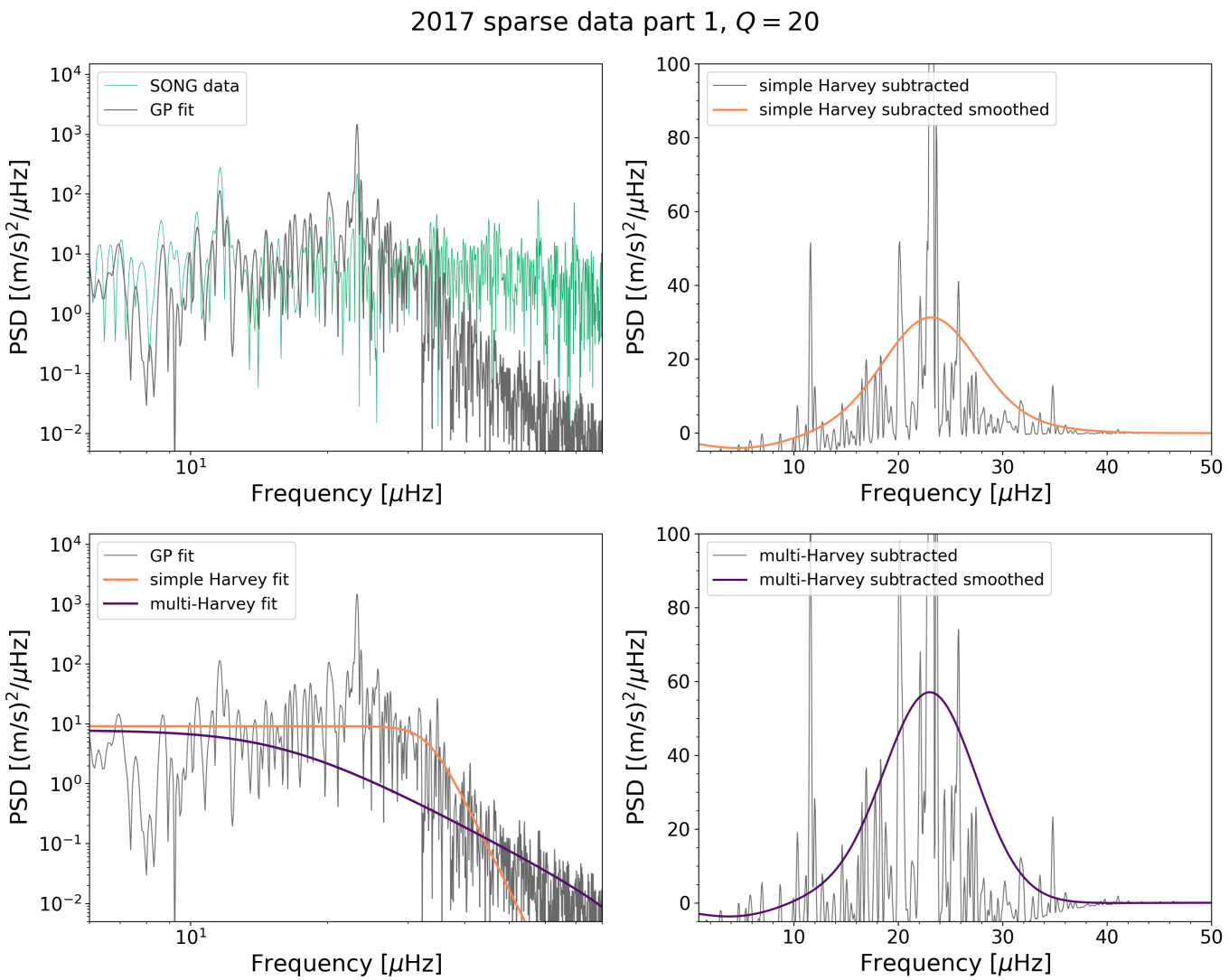

Fig. B.5. RV amplitude determination of the sparse section part 1 with Q = 18 of the 2017 SONG observations, the corresponding RV is shown in the top panel of Fig. B.2.

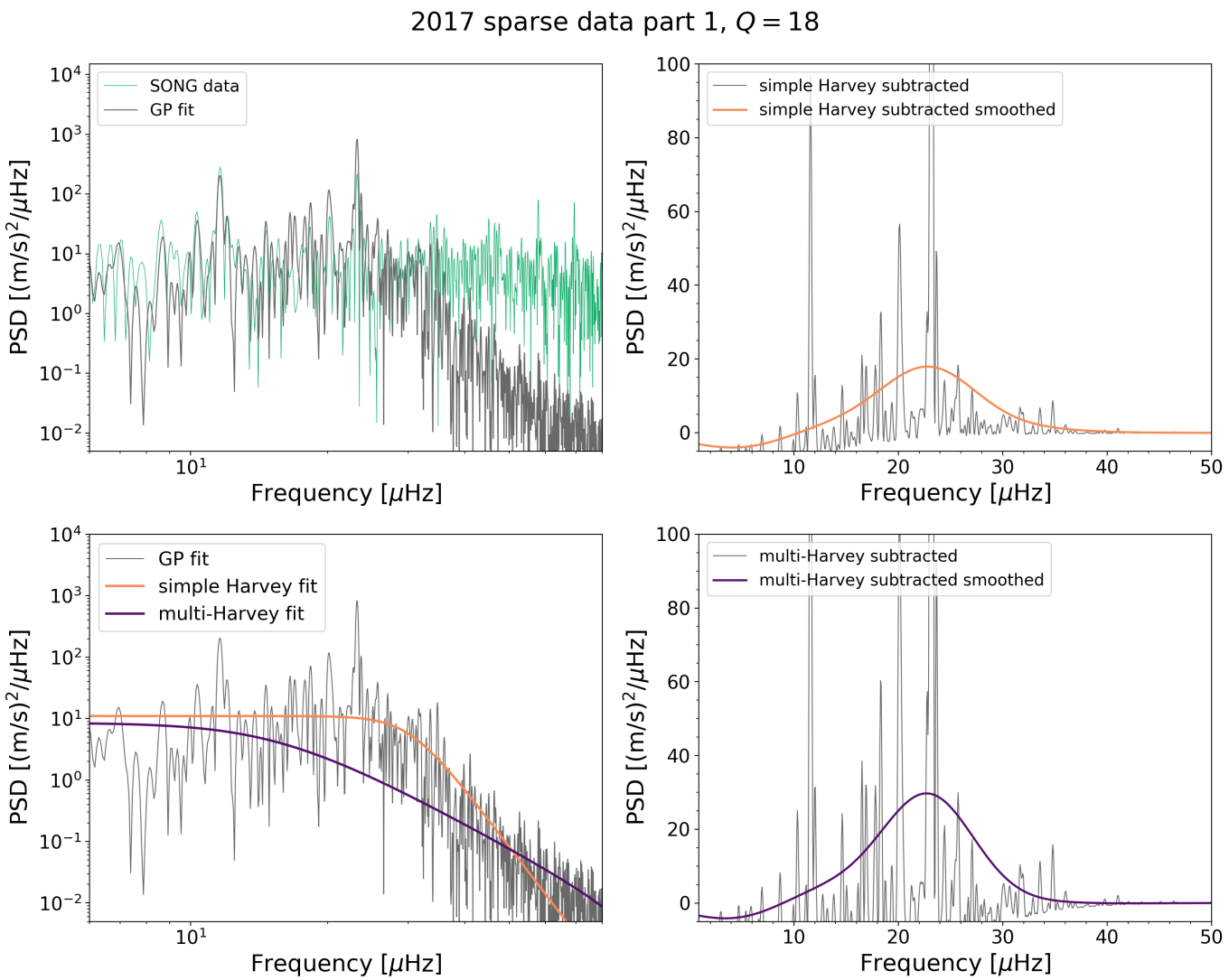

Fig. B.6. RV amplitude determination of the sparse section part 1 with Q = 20 of the 2017 SONG observations, the corresponding RV is shown in the middle panel of Fig. B.2.

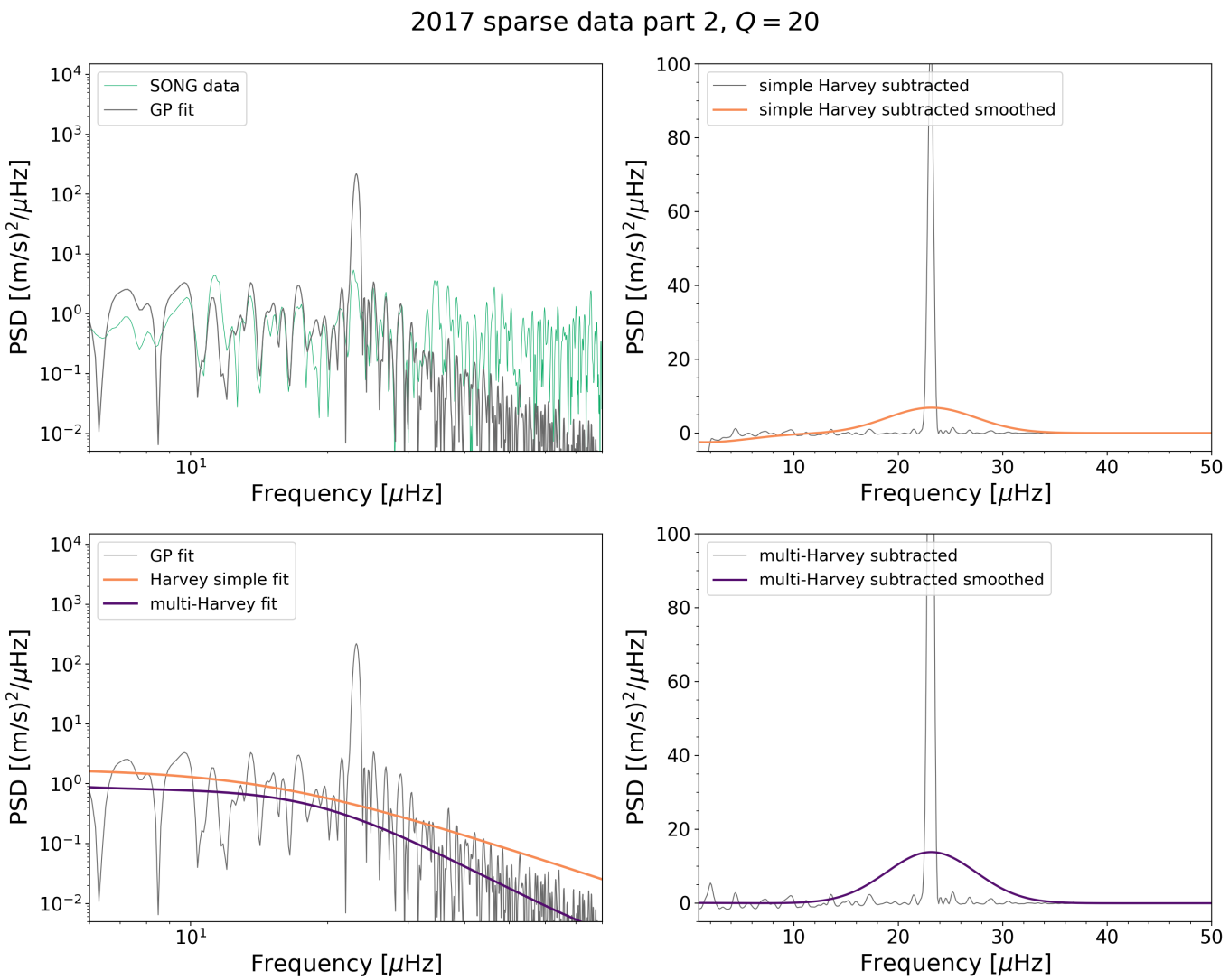

Fig. B.7. RV amplitude determination of the sparse section part 2 of the 2017 SONG observations, the corresponding RV is shown in the bottom panel of Fig. B.2.

Name	$T_{\rm eff}$ [K]	Mass [$M_\odot$]	$\nu_{\rm max}$ [μHz]	$A_{\rm vel}$ [cm/s]
β Aql A	5155 ± 15	1.24 ± 0.02	425 ± 5	49.7 ± 4.4
HD188512	Soubiran et al. (2022)	Kjeldsen et al. (2025)	Kjeldsen et al. (2025)	Kjeldsen et al. (2025)
α Cen A	5804 ± 13	1.0788 ± 0.0029	2400 ± 240	22.5
	Soubiran et al. (2022)	Akeson et al. (2021)	Kjeldsen et al. (2008)	Kjeldsen et al. (2008)
α Cen B	5207 ± 12	0.9092 ± 0.0025	4100 ± 410	7.2
	Soubiran et al. (2022)	Akeson et al. (2021)	Kjeldsen et al. (2008)	Kjeldsen et al. (2008)
τ Cet	5339 ± 19	0.783 ± 0.012	4490 ± 100	11.2 ± 0.8
HD10700	Hojjatpanah et al. (2019)	Teixeira et al. (2009)	Teixeira et al. (2009)	Teixeira et al. (2009)
α For A	6240	1.33 ± 0.01	1100 ± 110	34.8 ± 0.9
HD20010A	Santos et al. (2001)	Santos et al. (2001)	Kjeldsen et al. (2008)	Kjeldsen et al. (2008)
β Hyi	5917 ± 25	1.127 ± 0.054	1000 ± 100	41.9 ± 0.9
HD2151	Soubiran et al. (2022)	Metcalfe et al. (2024)	Bedding et al. (2007)	Bedding et al. (2007)
ϵ Ind A	4700 ± 65	0.782 ± 0.023	5305 ± 176	2.6 ± 0.5
HD209100	Lundkvist et al. (2024)	Lundkvist et al. (2024)	Campante et al. (2024)	Campante et al. (2024)
ν Ind	5318 ± 80	0.85	320 ± 32	64.7 ± 0.9
HD211998	Fuhrmann & Chini (2021)	Fuhrmann & Chini (2021)	Bedding et al. (2006)	Kjeldsen et al. (2008)
70 Oph A	5370.31 ± 1	0.90 ± 0.10	4500 ± 500	13.9
HD165341	Piccotti et al. (2020)	Piccotti et al. (2020)	Carrier & Eggenberger (2006)	Carrier & Eggenberger (2006)
δ Pav	5609 ± 8	1.07 ± 0.01	2300 ± 300	19.5 ± 0.4
HD190248	Carvalho-Silva et al. (2025)	Carvalho-Silva et al. (2025)	Kjeldsen et al. (2008)	Kjeldsen et al. (2008)
18 Sco	5824 ± 30	1.01 ± 0.02	3000 ± 200	20
HD146233	Soubiran et al. (2024)	Karovicova et al. (2022)	Bazot et al. (2011)	Bazot et al. (2011)
γ Ser	6296 ± 16	1.21	1600 ± 160	34.2 ± 1.3
HD142860	Soubiran et al. (2022)	Aguilera-Gómez et al. (2018)	Kjeldsen et al. (2008)	Kjeldsen et al. (2008)
HD219134	4817 ± 62	0.763 ± 0.034	4651 ± 301	4.23 ± 0.41
	Rosenthal et al. (2021)	Li et al. (2025)	Li et al. (2025)	Li et al. (2025)
HD35833	5684 ± 65	1.42 ± 0.04	596 ± 17	111 ± 9
	Fouesneau et al. (2023)	Gupta et al. (2022)	Gupta et al. (2022)	Gupta et al. (2022)
Sun	5772	1	3100 ± 40	16.0 ± 0.4
	Prša et al. (2016b)		Hekker (2020)	Kjeldsen et al. (2025)

Table C.1. The astrophysical parameters of other stars we used for comparison in Figs. 7 and 8 with their respective references. Additionally to their names, we indicated their Henry Draper Catalogue ID, if applicable.